ADVANCED FUNCTIONAL MATERIALS
www.afm-journal.de

Controlling Magneto-Ionics by Defect Engineering Through Light Ion Implantation

Zheng Ma, Sofia Martins, Zhengwei Tan, Song Chen, Elmer Monteblanco, Maciej O. Liedke, Maik Butterling, Ahmed G. Attallah, Eric Hirschmann, Andreas Wagner, Alberto Quintana, Eva Pellicer, Dafiné Ravelosona, Jordi Sort,* and Enric Menéndez**

Magneto-ionics relies on the voltage-driven transport of ions to modify magnetic properties. As a diffusion-controlled mechanism, defects play a central role in determining ion motion and, hence, magneto-ionic response. Here, the potential of ion implantation is exploited to engineer depth-resolved defect type and density with the aim to control the magneto-ionic behavior of Co_3O_4 thin films. It is demonstrated that through a single implantation process of light ions (He^+) at 5 keV, the magneto-ionic response of a nanostructured 50 nm thick Co_3O_4 film, in terms of rate and amount of induced magnetization, at short-, mid-, and long-term voltage actuation, can be controlled by varying the generated collisional damage through the ion fluence. These results constitute a proof-of-principle that paves the way to further use ion implantation (tuning the ion nature, energy, fluence, target temperature, or using multiple implantations) to enhance performance in magneto-ionic systems, with implications in ionic-based devices.

1. Introduction

The ever-growing demands on fast and efficient data processing and storage, driven by Big Data, are pushing information technology to its performance limits; particularly, energy efficiency remains to be a major bottle-neck in current computing paradigms.[1] Although artificial intelligence is showing success to tackle Big Data requests, this is mainly achieved by software means, thus at a cost of a large energy consumption. Artificial intelligence is at a turning point and requires low-power technologies to build new computing hardware.[2,3] Voltage control of magnetism (VCM) holds the potential to revolutionize computing from an energy-efficiency standpoint since it enables the modification of magnetic properties by electric fields instead of electric currents, decreasing Joule heating effect and, ultimately, resulting in a much-reduced power consumption.[1,4–8] Among VCM mechanisms,[1,4–6] electric-field-induced ion motion to modulate magnetism of a target material (magneto-ionics) stands out since it allows for a voltage-driven tailoring magnetic properties to an extent never reached by any other VCM means.[7,8] Extensive studies have been performed to compare mobile ion species of different nature (e.g., H^+,[9–14] Li^+,[15–18] N^{3-},[19–24] O^{2-}[25–32] or F^-[33]), dissimilar magneto-ionic targets and layered architectures (e.g., adjacent reservoirs to provide/sink ions to/from the target versus targets in which the mobile ions are already present in it), and distinct approaches to apply electric field (e.g., solid-state electrolytes[9,26,27] versus the formation of an electric double layer through liquid electrolytes).[19–23,28–30] Remarkably, while

Z. Ma, S. Martins, Z. Tan, E. Pellicer, J. Sort, E. Menéndez
Departament de Física
Universitat Autònoma de Barcelona
Cerdanyola del Vallès E-08193, Spain
E-mail: jordi.sort@uab.cat; enric.menendez@uab.cat

S. Chen, D. Ravelosona
Centre de Nanosciences et de Nanotechnologies
CNRS
Université Paris-Saclay
10 Boulevard Thomas Gobert, Palaiseau 91120, France
E-mail: dafine.ravelosona@spin-ion.com

The ORCID identification number(s) for the author(s) of this article can be found under https://doi.org/10.1002/adfm.202312827

DOI: 10.1002/adfm.202312827

E. Monteblanco, D. Ravelosona
Spin-Ion Technologies
10 Boulevard Thomas Gobert, Palaiseau 91120, France

M. O. Liedke, M. Butterling, A. G. Attallah, E. Hirschmann, A. Wagner
Institute of Radiation Physics
Helmholtz-Zentrum Dresden – Rossendorf
01328 Dresden, Germany

A. Quintana
Institut de Ciència de Materials de Barcelona (ICMAB-CSIC)
Universitat Autònoma de Barcelona
Campus UAB
Bellaterra, Barcelona E-08193, Spain

J. Sort
Institució Catalana de Recerca i Estudis Avançats (ICREA)
Pg. Lluís Companys 23, Barcelona E-08010, Spain

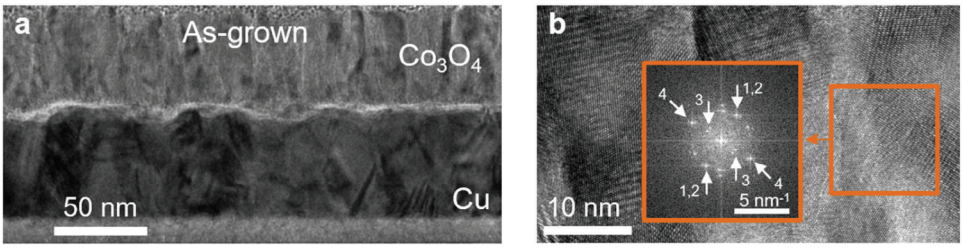

Figure 1. Structural characterization of the Co_3O_4 films by transmission electron microscopy (TEM): a) TEM image of the cross-section of an as-grown Co_3O_4 film. b) High-resolution TEM image of a region of the cross-section of the Co_3O_4 layer imaged in a, which includes the fast Fourier transform of the region enclosed in the orange square. "1" and "2" spots are consistent with (311) Co_3O_4 (PDF 00-009-0418) and (111) CoO (PDF 00-001-1227) interplanar distances (0.244 and 0.245 nm, respectively), while spots "3" and "4" are unambiguously ascribed to (111) Co_3O_4 (PDF 00-009-0418) and (200) CoO (PDF 00-001-1227) interplanar distances (0.467 and 0.212 nm, respectively).

structural defects may also have a strong influence on ion diffusion in solids, generally enhancing ionic motion,[8,19,28,34–37] so far this effect has been much less investigated. In fact, not only the defect type and density play a role in ion migration but also their depth distribution.[37] Thus, magneto-ionic systems could largely benefit from a controlled defect type, density, and distribution along depth. Even though defect manipulation remains challenging, ion implantation at energies <100 keV turns out to be a particularly suitable approach to modify materials in the sub-100 nm depth range from structural and compositional viewpoints.[38] Ion implantation has already been used to tune magnetic properties,[39] such as magnetic anisotropy,[40] saturation magnetization by order-disorder transitions[41] or phase transformations,[42] ferromagnetic/antiferromagnetic coupling,[43] synthesis of composite multiferroics,[44] or more recently, formation and control of skyrmions.[45] In fact, light noble gas ion implantation has been largely used since it allows modifying magnetic properties without altering the composition of the target material or causing significant erosion of the sample surface.[39] However, its potential to engineer defects in terms of size, density, and distribution (i.e., with depth resolution) aimed at enhancing ion motion and induced magnetization through magneto-ionics has been largely overlooked.[46]

Here, we show that, by the interplay between the high defect density of the magneto-ionic target (i.e., nanostructured 50 nm thick Co_3O_4 film) and an implantation process using light ions (He^+) at 5 keV, the magneto-ionic response, in terms of rate and amount of induced magnetization, of the Co_3O_4 film at short- (< 2 min), mid- (2–8 min), and long-term (>8 min) voltage actuation can be controlled by varying the generated collisional damage through ion fluence. Co_3O_4, on top of offering a wide variety of defect frameworks (e.g., vacancy clusters, type of grain boundaries, etc.), allows for magneto-ionically driven ON–OFF ferromagnetism,[19,28] becoming a model system for both fundamental and technological research domains.

2. Results and Discussion

2.1. Growth and Characterization of as-Grown Magneto-Ionic Targets (Co_3O_4 films)

Fifty nanometers thick Co_3O_4 films were grown atop (100)-oriented Si substrates, previously coated with 20 nm of Ti and 60 nm of Cu, by reactive sputtering (see Experimental Section for further details). Depositions were carried out while partly masking the Cu/Ti buffer layers to serve afterward as working electrodes for the magnetoelectric characterization. As seen in **Figure 1a**, the Co_3O_4 film is nanostructured with rather elongated grains along the perpendicular direction to the film plane. This columnar-shaped growth has already been evidenced in thicker Co_3O_4 films grown by atomic layer deposition,[28] which is a much slower deposition technique compared to reactive sputtering, thus suggesting the tendency of Co_3O_4 to grow in such fashion. Figure 1b is a high-resolution transmission electron microscopy (TEM) image of the cross-section of the Co_3O_4 layer, which includes the fast Fourier transform (FFT) of the region marked with an orange square. Spots labeled as "1" and "2" are consistent with (311) Co_3O_4 (PDF 00-009-0418) and (111) CoO (PDF 00-001-1227) reflections, with interplanar distances 0.244 and 0.245 nm, respectively, whereas spots "3" and "4" are unambiguously ascribed to (111) Co_3O_4 (PDF 00-009-0418) and (200) CoO (PDF 00-001-1227) reflections, with interplanar distances 0.467 and 0.212 nm, respectively. This indicates that the as-grown films consist of a mixture of Co_3O_4 and CoO phases in agreement with previously reported results.[30] This is linked to the role of the Cu buffer layer which also might suffer from oxidation while depositing (as evidenced by the brightness of the Co_3O_4-Cu interface in Figure 1a), effectively yielding a decreased oxygen partial pressure, which promotes the growth of CoO over Co_3O_4 during the first growth stages. This effect weakens as the thickness increases and then Co_3O_4 grows preferentially.[30] For simplicity, the films are denoted as Co_3O_4 along the text.

Defect characterization at atomic level by means of variable energy positron annihilation lifetime spectroscopy (VEPALS)[47–51] reveals that roughly two "sublayers" with different defect sizes and densities can be distinguished across the thickness of the as-grown Co_3O_4 films. PALS provides the positron lifetime τ, which is a measure of defect size and, thus, of defect type, as a function of the depth of the investigated material. Three representative defect dimensions, known as lifetime components τ_i (where $i = 1$, 2, or 3), can be characterized. The shortest lifetime component τ_1 represents here smaller vacancy clusters, the intermediate lifetime component τ_2 accounts for larger vacancy clusters linked to grain boundaries or small pores in case of the largest values, and the longest lifetime component τ_3 is attributed to even larger pores or voids. Each component has a corresponding relative intensity (I_i) which to some extent reflects the concentration of each

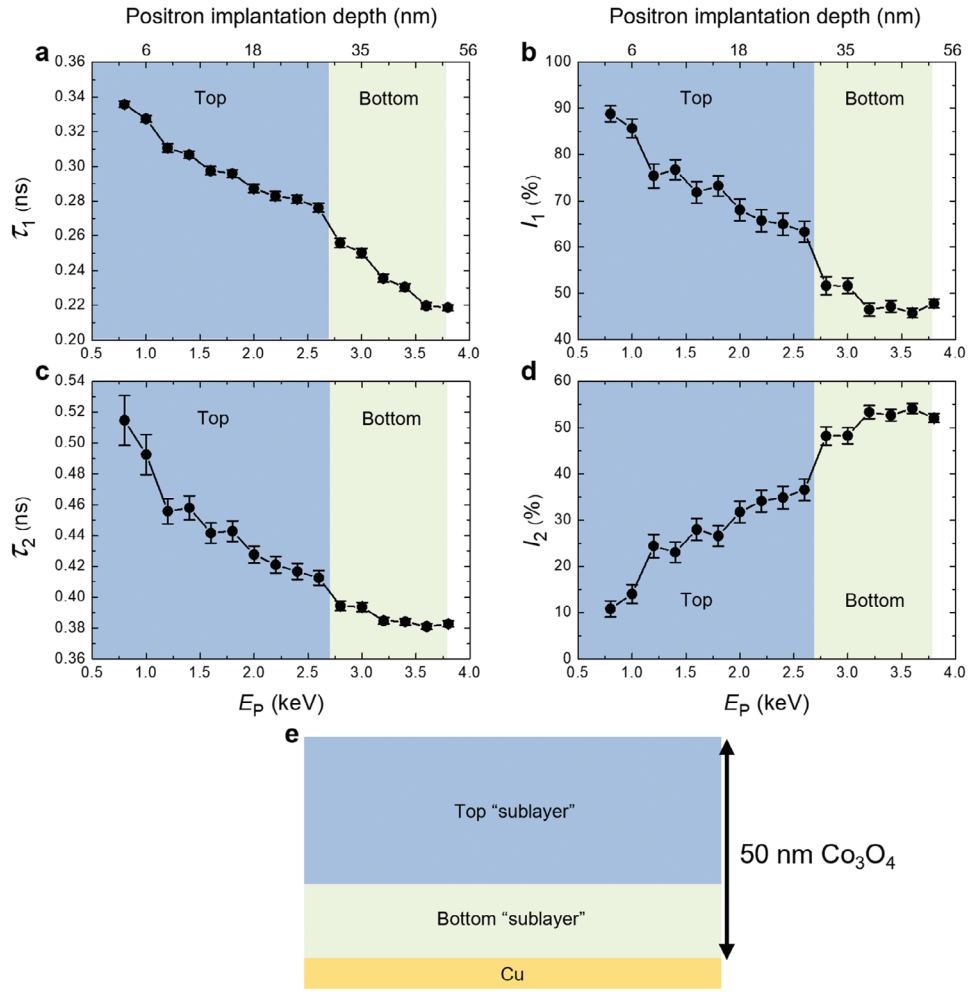

Figure 2. Depth-resolved defect characterization of the as-grown Co_3O_4 films by variable energy positron annihilation lifetime spectroscopy (VEPALS): a) and b) are the positron lifetime component 1 (τ_1) and the corresponding relative intensity (I_1), respectively, as a function of positron implantation depth, which can be also given in positron implantation energy (E_P). See the Experimental Section for further details. c) and d) are the positron lifetime component 2 (τ_2) and the corresponding relative intensity (I_2), respectively, as a function of positron implantation depth. The blue and green shadings account for the two "sublayers" that can be distinguished from a defect standpoint. The lines connecting data points are guides to the eye. e) is a schematic of the sample along depth.

defect type.[47–51] **Figure 2** shows the depth-dependence of τ_1 and τ_2 and the corresponding relative intensities, I_1 and I_2, respectively. At each depth, the sum of I_1 and I_2 is very close to 100%, indicating that the contribution from τ_3 is virtually negligible, in agreement with the absence of voids in the TEM characterization of the cross-section of the as-grown Co_3O_4 film (Figure 1). Positron lifetimes might be overestimated along the top part of the Co_3O_4 film due to the influence of roughness and surface broken symmetry, becoming negligible at depths above 20 nm (>2 keV in terms of positron implantation energy, E_P); see Experimental Section for further details.[52] At depths above 20 nm (>2 keV), positron lifetimes can be considered fully representative of the Co_3O_4 film. With increasing depth, τ_1, τ_2, and I_1 decrease, while I_2 increases (all in a monotonic way). However, all suffer from a more pronounced change (i.e., a jump in the trend) between 2.6 and 2.8 keV (which represent depths of ≈28 and 31 nm, respectively). This could be linked to an interface region amongst two "sublayers" with different defect sizes and densities. As reported in reference 30, the Cu buffer layer, which acts as bottom electrode, tends to promote the growth of CoO over Co_3O_4 during the first stages of Co oxide deposition. The influence of the Cu electrode on the Co oxide growth weakens with thickness, extending up to the first 20 nm of the film, in agreement with the depth of the border between the two "sublayers" evidenced by VEPALS. This indicates that the origin of the two "sublayers" is related to the role of the Cu buffer layer to slightly react with oxygen during the Co oxide growth. A similar jump of data points is also visible near the surface, specifically between positron implantation energies of 1 and 1.2 keV (which represent depths of around 6 and 8 nm, respectively). The origin of the jumps is at least partly related to the stronger influence of the defect microstructure of the top surface on the first jump rather than on the second one. In general, the top surface of a film shows a different defect microstructure than the rest of the film due to factors like roughness and surface broken symmetry, which result in a higher density of defects and a larger

positronium formation.[53,54] The latter tends to increase positron lifetime. The influence of the defect microstructure of the top surface on positron lifetime weakens with depth, vanishing beyond the first 20 nm, and is responsible for the positron lifetime decrease with increasing depth. Thus, while the first jump might be affected by the influence of the defect microstructure of the very top surface, the second jump (deeper one) accounts exclusively for changes in defect size. Considering the defect size and density at 2.2 keV (21 nm) and 3.2 keV (39 nm) as representative values for the top and bottom "sublayers", respectively, the top region shows τ_1, τ_2, I_1, and I_2 values of 0.2829 ns, 0.4211 ns, 65.7%, and 34.1%, respectively, whereas the bottom counterpart exhibits τ_1, τ_2, I_1 and I_2 values of 0.2355 ns, 0.3848 ns, 46.5%, and 53.3%, respectively. Figure S1 (Supporting Information) shows the ab initio calculations of the positron lifetime in Co_3O_4 as a function of vacancy cluster size,[55–57] indicating that mixed vacancy cluster sizes of 10 and 4 vacancies are consistent with the τ_1 values of the top and bottom "sublayers", respectively. This agrees with the nanostructured nature of the sputtered Co_3O_4 film. In general, both TEM and VEPALS provide microstructural information but at different size scales. In contrast to TEM, VEPALS allows for a characterization at the atomic level.[58] This explains why the influence of implantation fluence on the microstructure is barely observed by TEM, whereas VEPALS differences are significant. Thus, a correlation between TEM and VEPALS results is not always straightforward as it happens in these systems. Remarkably, τ_2 values are not so much larger than τ_1 ones, suggesting that both components might represent the same defect type, that is, mixed vacancy clusters which could be linked to grain boundaries with different sizes. This is in concordance with the TEM characterization where grain boundaries are clearly observed (Figure 1).

2.2. Defect Engineering Through Light Ion Implantation

Controlling defect type (size), density, and distribution is central for ion diffusion. Typically, ion transport becomes enhanced with increasing defect size (as it happens with grain boundaries compared to the bulk of the grains) and density.[34–36] Defect manipulation with depth-resolution remains challenging. The first attempt to tailor the defect structure relies on the growth method. For instance, growing Co_3O_4 by reactive sputtering tends to result in larger defect sizes than Co_3O_4 grown by techniques that involve slower deposition rates, such as atomic layer deposition.[28] However, further control of the microstructure is strongly required to tune ion diffusion. Aimed at further tailoring defect type and density along depth, ion implantation at energies of the order of 1–100 keV turns out to be particularly suitable to modify materials in the sub-100 nm depth range from structural and compositional viewpoints.[38] In a first approximation, the penetration of ions is controlled by their energy, while implantation damage (also known as collisional damage) is determined by the fluence.[38] Typically, in ion implantation processes into crystalline materials, impinging ions collide with lattice atoms, displacing them from their equilibrium lattice sites and, for instance, forming vacancies. With increasing fluence, these vacancies may grow forming vacancy clusters, grain boundaries and, eventually, disordered regions.[38] However, a completely different scenario in terms of collisional damage emerges when the implantation target is already highly defective, enabling new mechanisms of ion-solid interactions.[59–61] Even though not so much is known about the interaction of preexisting defects with impinging ions,[61] theoretical calculations by molecular dynamics report on the role of implantation fluence in determining the size of preexisting defects.[60] In fact, nanopore size reduction has been reported by 3 keV Ar ion implantation at normal incidence into amorphous-like materials.[59] Recently, it has been shown that, with ion fluence leading to collisional damages up to 0.1 dpa (displacement per atom), the density of small vacancy clusters increases while the size of pores reduces significantly in highly defective Fe films upon 2 MeV Fe ion implantation at normal incidence.[61] Inspired by these results and considering the highly defective nature of the as-grown Co_3O_4 films, 5 keV He ion implantation with a fluence of 10^{15} ion cm^{-2} was used to achieve maximum collisional damage of ≈0.1 dpa (**Figure 3**). The ion energy of 5 keV was adjusted to have the maximum collisional damage located at a depth around 18 nm (i.e., within the top "sublayer") to avoid a pronounced atomic intermixing at the

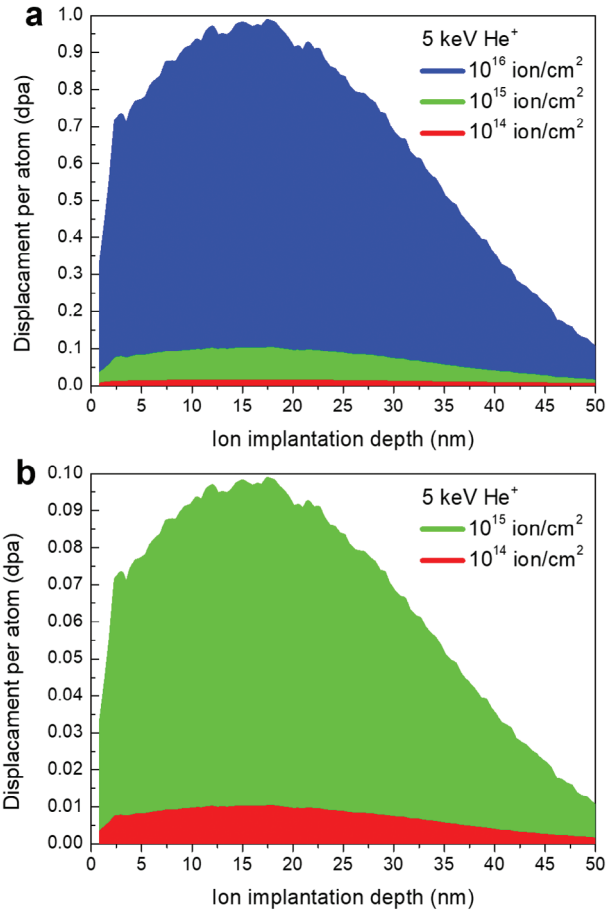

Figure 3. Depth-resolved collisional damage profiles given as displacement per atom (dpa) caused by 5 keV He ion implantation into Co_3O_4: a) Depth-resolved collisional damage for the three used fluences: 10^{14}, 10^{15}, and 10^{16} ion cm^{-2}. b) Depth-resolved collisional damage for the 10^{14} and 10^{15} ion cm^{-2} fluences to better visualize dpa values along Co_3O_4 depth. These results are obtained from the TRIM simulation presented in Figure S2 (Supporting Information).[62]

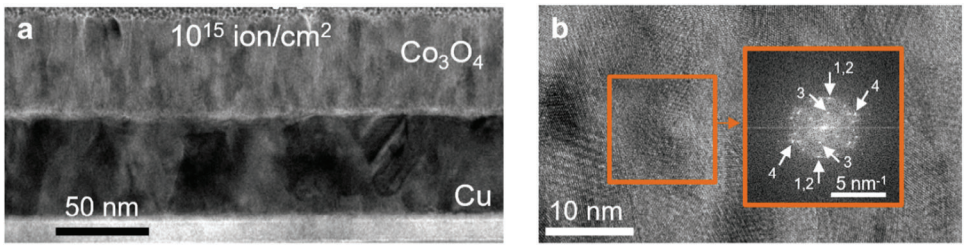

Figure 4. Structural characterization of a Co_3O_4 film implanted with 5 keV He ions to a fluence of 10^{15} ion cm^{-2} by transmission electron microscopy (TEM): a) TEM image of the cross-section of a Co_3O_4 film implanted with 5 keV He ions with a fluence of 10^{15} ion cm^{-2}. b) High-resolution TEM image of a region of the cross-section of the implanted Co_3O_4 layer imaged in (a), which includes the fast Fourier transform of the region enclosed in the orange square. "1" and "2" spots are consistent with (311) Co_3O_4 (PDF 00-009-0418) and (111) CoO (PDF 00-001-1227) interplanar distances (0.244 and 0.245 nm, respectively), while spots "3" and "4" are unambiguously ascribed to (111) Co_3O_4 (PDF 00-009-0418) and (200) CoO (PDF 00-001-1227) interplanar distances (0.467 and 0.212 nm, respectively).

Cu interface which could be detrimental to the conductivity of the Cu bottom electrode. This would negatively affect the magneto-ionic performance of the implanted film. He ion implantation to fluences of 10^{14} and 10^{16} ion cm^{-2} were also carried out to achieve degrees of collisional damage much below and much above 0.1 dpa (10^{-2} and 1 dpa, respectively). Light noble He ions were chosen to avoid compositional changes in the Co_3O_4 film and minimize film sputtering. Figure 3 shows how collisional damage evolves across the Co_3O_4 film for the fluences used. This is calculated from the collisional damage profiles given in number of displacements per impinging ion and crossed distance (Figure S2, Supporting Information) simulated by the TRIM (TRansport of Ions in Matter) program.[62] From these results, which depend on the implantation target, ion type, charge, and energy, dpa at each depth for the used fluences can be obtained by multiplying the fluence by the number of displacements per impinging ion and the crossed distance and then dividing the obtained result by the atomic density of the target material. A unit of 1 dpa means that, on average, every atom in the implanted volume has been displaced once from its equilibrium lattice site.

As seen from the TEM images of the cross-section of the implanted film (**Figure 4**), 5 keV He ion implantation with a fluence of 10^{15} ion cm^{-2} into 50 nm thick Co_3O_4 layer results in virtually no sputtering of the Co_3O_4 film (as it happens with the film implanted with 10^{16} ion cm^{-2}, see Figure S3, Supporting Information). Even though no pronounced microstructural differences are found compared to the as-grown film (cf. Figures 1 and 4; Figure S4, Supporting Information), boundaries between elongated grains become blurred (i.e., less well-defined).

To investigate how the Co_3O_4 microstructure evolves with ion implantation fluence at atomic level, a depth-resolved defect characterization (**Figure 5**) was carried out by means of Doppler broadening variable energy positron annihilation spectroscopy (DBVEPAS),[47,48] and VEPALS.[47–51] DBVEPAS allows for investigating microstructures mainly from a defect concentration viewpoint, whereas VEPALS offers the possibility to precisely assess defect size. Figure 5a shows the evolution of the *S* parameter with depth, which strongly varies with ion fluence, confirming the role of ion implantation in modifying the defect size and density. The *S* parameter is the fraction of positrons annihilating with low momentum valence electrons and represents vacancy-type defects and their concentration. Defect size and density are convoluted in *S* and, thus, compensation effects might occur in systems where defect size varies oppositely to the defect density (i.e., while one increases, the other decreases or vice versa). However, it is generally accepted that *S* is most sensitive to defect concentration since it accounts for the valence electron fraction.[47] As shown in Figure 2, the VEPALS characterization of an as-grown Co_3O_4 film suggests the existence of two "sublayers" with different defect sizes and densities within the film. Remarkably, this "double layer" structure (denoted as top and bottom "sublayers" throughout the text) is also detectable from the *S* parameter depth profile (Figure 5a), where a relative maximum at $E_p = 2.6$ keV is observed. Within the top sublayer, the *S* parameter (Figure 5a) significantly varies with ion fluence, increasing for the film implanted with 10^{14} ion cm^{-2}, but, subsequently, decreasing with increasing fluence down to values far below those of the as-grown state for the film implanted with 10^{16} ion cm^2. Within the bottom layer, even though the changes of the *S* parameter with increasing fluence are less pronounced, it also tends to decrease for the films implanted with 10^{15} and 10^{16} ion cm^{-2}, which is in line with a concomitant change of the average positron lifetime (Figure 5b).

In contrast to DBVEPAS, VEPALS allows determining defect size and to some extent defect concentration as a function of depth. As seen in Figure 5b, the average lifetime $\tau_{Average}$ decreases monotonically with increasing depth. Moreover, the average lifetime $\tau_{Average}$ also reduces with increasing ion fluence, except for the top 13 nm (which corresponds to a positron implantation energy of 1.6 keV), where an implantation with 10^{14} ion cm^{-2} slightly increases $\tau_{Average}$ compared to the as-grown sample. This evidences that at such low fluence ion implantation leads to the usual effect of enlarging defect size, suggesting that a threshold fluence might be required to enable the abovementioned new mechanisms of ion-solid interactions that result in a decreased defect size with increasing implantation fluence. In general, the top surface of a film shows a different defect microstructure than the rest of the film and its influence on the positron lifetime weakens with depth, tending to vanish beyond the first 20 nm. This behavior is responsible for the decrease with increasing depth of both the S parameter and the positron lifetime. Within the top "sublayer" and particularly among the first nm, where the influence of the defect microstructure is the most intense, the more pronounced increase of the *S* parameter compared to the average positron lifetime for the film implanted with 10^{14} ion cm^{-2} is a consequence of the larger sensitivity of DBVEPAS to defect concentration, compared to VEPALS.[63] Figure 5c,d,

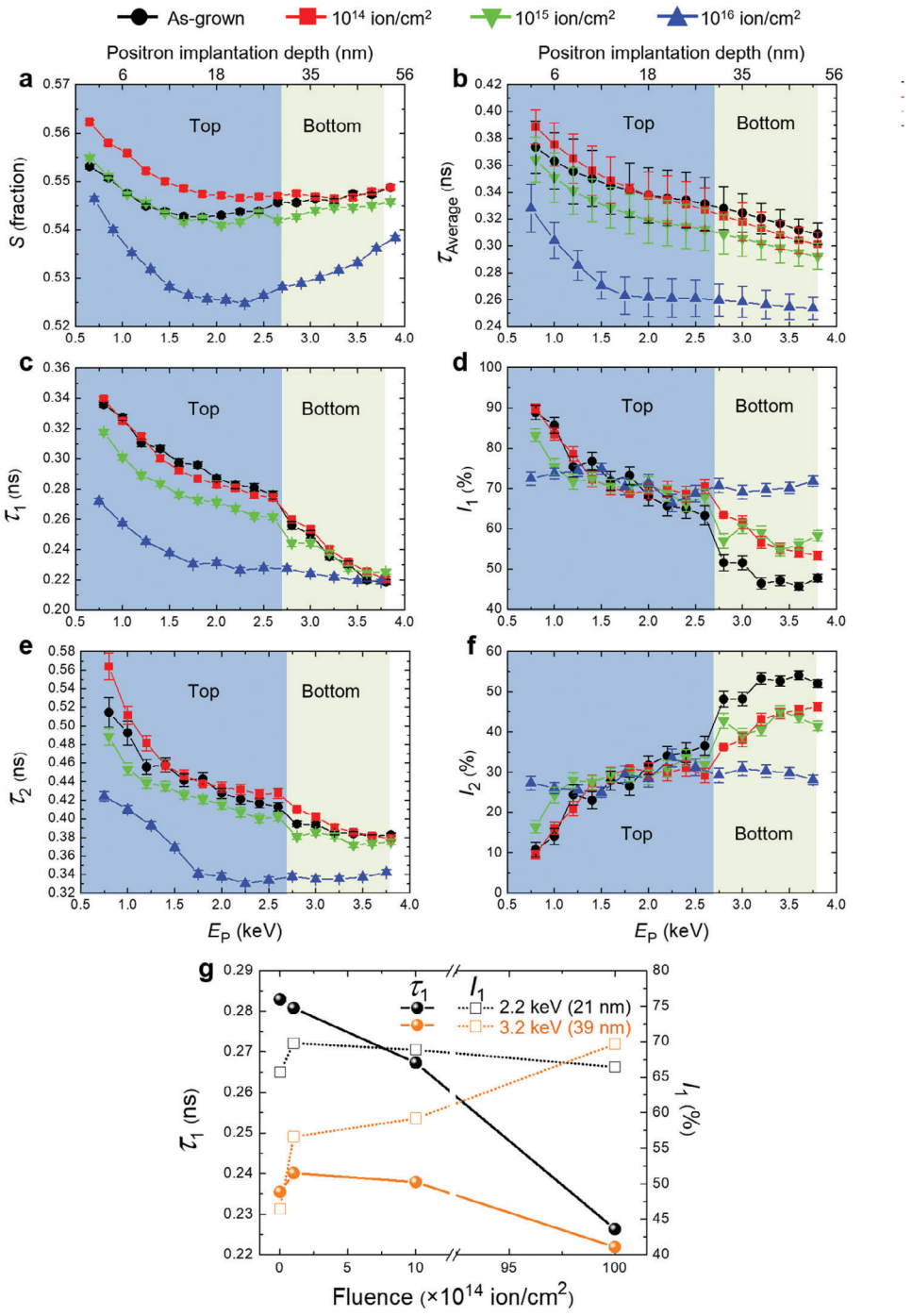

Figure 5. Depth-resolved defect characterization of as-grown and implanted Co_3O_4 films by Doppler broadening variable energy positron annihilation spectroscopy (DBVEPAS) and variable energy positron annihilation lifetime spectroscopy (VEPALS): a) *S* parameter obtained by DBVEPAS characterization as a function of positron implantation depth which can be also given in positron implantation energy (E_P). See Experimental Section for further details. b) Average lifetimes obtained by VEPALS as a function of positron implantation depth. c) and d) are the positron lifetime components 1 (τ_1) and the corresponding relative intensities (I_1), respectively, as a function of positron implantation depth. e) and f) are the positron lifetime components 2 (τ_2) and the corresponding relative intensities (I_2), respectively, as a function of positron implantation depth. g) represents the evolution of τ_1 and I_1 as a function of ion fluence at two representative Co_3O_4 depths of both top and bottom "sublayers", represented by a blue and a green rectangle in the background, respectively. The lines connecting data points are guides to the eye.

shows the depth-dependence of the positron lifetime component 1 (τ_1) and the corresponding relative intensity (I_1), respectively, whereas Figure 5e,f exhibit the positron lifetime component 2 (τ_2) and the corresponding relative intensity (I_2), respectively. As seen in Figure 5c, the depth-resolved evolution of τ_1 of the film implanted with 10^{14} ion cm^2 overlaps with that of the as-grown film, indicating that at such fluence mixed vacancy cluster of ≈4 vacancies remains unaltered in size. Conversely, upon implanting with 10^{15} ion cm^{-2}, the size of vacancy clusters decreases, and this reduction becomes much more pronounced after implanting with 10^{16} ion cm^{-2}. As it happens in other systems, this decrease of defect size with implantation fluence might be related to the flow of implantation-induced interstitials toward vacancy clusters and grain boundaries, which subsequently shrink in size.[61] Remarkably, except for the film implanted with 10^{16} ion cm^{-2}, from a depth of ≈39 nm (3.2 keV) on, the values of τ_1 overlap for all films, in agreement with the localized implantation damage profile within the top part of the film. Interestingly, the relative intensity I_1 follows an opposite behavior: it remains rather unaltered (being τ_1 the dominant defect size since the lowest value is above 60%) with increasing fluence up to depths of ≈28 nm (2.6 keV). At further depths, I_1 tends to increase with increasing fluence, which possibly indicates a reduction of open volumes due to ion implantation in the top part of the film leading to a larger number of positrons being able to reach the bottom layer (in agreement with the fluence evolution of S in Figure 5a). With respect to τ_2, the implanted film with 10^{14} ion cm^{-2} shows slightly larger values than the as-grown film. However, for fluences of 10^{15} and 10^{16} ion cm^{-2}, τ_2 decreases with increasing fluence. As happens with τ_1 and I_1, τ_2 values (except for the film implanted with 10^{16} ion cm^{-2}) also tend to overlap at a depth of ≈39 nm (3.2 keV), and I_2 remains rather unchanged with increasing fluence up to depths of ≈28 nm (2.6 keV). At further depths, in contrast to I_1, I_2 tends to decrease with increasing fluence. However, for implanted samples, the density of mixed vacancy clusters with a number of vacancies <10 is dominant (I_1 > 50%) compared to larger vacancy clusters. This together with the TEM results suggest that the grain boundaries observed by TEM upon implantation might have slightly narrowed (see Figures S3 and S4, Supporting Information). Since small mixed vacancy clusters are dominant over large mixed vacancy clusters, a detailed evolution of τ_1 and I_1 with increasing fluence is shown for the two different "sublayers" in Figure 5g. Here, one can see the overall effect of ion implantation, which tends to decrease defect size while keeping a similar defect density in the top "sublayer" (a small drop of I_1 with fluence is likely related to the lower trapping efficiency of smaller vacancy clusters). On the other hand, in the bottom "sublayer", the trends become opposite: defect size (τ_1) remains rather unaltered and defect density (I_1) increases with increasing fluence. As discussed, the former is likely a consequence of the overall defect density reduction (smaller positron trapping potentials) in the top "sublayer", hence leading to a larger positron diffusion length. Remarkably, given a nanostructured film (which enables mechanisms of ion-solid interactions that result in defect shrinking with increasing fluence),[61] depth-resolved defect structure can be engineered with a fluence window from 10^{14} to 10^{16} ion cm^{-2} with a single ion implantation process. The film implanted with 10^{16} ion cm^{-2} results in a completely different defect scenario from the rest of the samples, which is characterized by a much reduced average defect size.

2.3. Magneto-Ionic Behavior

To investigate the magneto-ionic behavior of the films, magnetoelectric measurements were carried out by vibrating sample magnetometry while electrolyte-gating the films (see Experimental Section for further details).[64,65] Specifically, the magnetization M as a function of time t was obtained under gating at −50 V for 30 min while externally applying an in-plane magnetic field of 10 000 Oe (i.e., 1 T) to ensure that the induced magnetization remains saturated, thus enabling determination of saturation magnetization (M_S) versus time (t): M_S (t) as shown in **Figure 6a**. The as-grown film shows a rather typical magneto-ionic response characterized by a gradual increase of M_S due to both the migration of O ions toward the liquid electrolyte, which acts as ion reservoir, and O ion redistribution within the film, leaving behind Co-rich areas that account for the generated ferromagnetism.[28] The as-grown and all implanted Co_3O_4 films are overall paramagnetic with traces of ferromagnetism likely ascribed to impurities in the Si substrate (Figure S5, Supporting Information). Interestingly, implantation fluence has a very strong impact on the dependence of M_S versus t. Using the behavior of the non-implanted film as a reference, at an initial stage of voltage actuation (i.e., first 2 min approximately), the film implanted with a fluence of 10^{14} ion cm^{-2} shows a larger magneto-ionic rate, whereas that implanted with 10^{15} ion cm^{-2} exhibits a much slower one as seen by the slope of the M_S versus t. For instance, after actuating for 30 s (i.e., t = 5.5 min), the slope of the curve in Figure 6a varies from around 20 (10^{14} ion cm^{-2}) to 9 (as-grown) and 4 emu·cm^{-3}·min^{-1} (10^{15} ion cm^{-2}). The magnitude of the slopes agrees with previously reported results on this system.[30] In this initial stage, the film implanted with 10^{16} ion cm^{-2} barely shows magneto-ionic effect, indicating that this is suppressed and/or delayed. After this initial stage, both the as-grown and the film implanted with 10^{14} ion cm^{-2} show a rather similar M_S evolution with t up to 8 min of voltage actuation. Conversely, in this time window, the film implanted with 10^{15} ion cm^{-2} shows lower saturation magnetization values but an increased slope, reaching the same M_S at 8 min as the as-grown film and that implanted with 10^{14} ion cm^{-2}. Moreover, while the as-grown film tends to saturate, the films implanted with 10^{14} and 10^{15} ion cm^{-2} keep on growing their M_S without leveling off, generating much larger magnetizations. At 30 min of voltage actuation, M_S values of 220, 314, 465, and 92 emu cm^{-3} are reached for the as-grown and films implanted with 10^{14}, 10^{15}, and 10^{16} ion cm^{-2}, respectively. To summarize, taking the magneto-ionic behavior of the as-grown film as a reference, low fluences (i.e., 10^{14} ion cm^{-2}) result in both slightly larger magneto-ionic rates and generated saturation magnetization at short and long voltage actuation times, respectively. Intermediate fluences (i.e., 10^{15} ion cm^{-2}) lead to smaller magneto-ionic rates but the largest generated saturation magnetization at short and long voltage actuation times, respectively. Finally, at high fluences, the magneto-ionic effect becomes rather restricted in both the rate and amount of induced magnetization. Figure 6b–e shows the first two consecutive magnetization versus applied

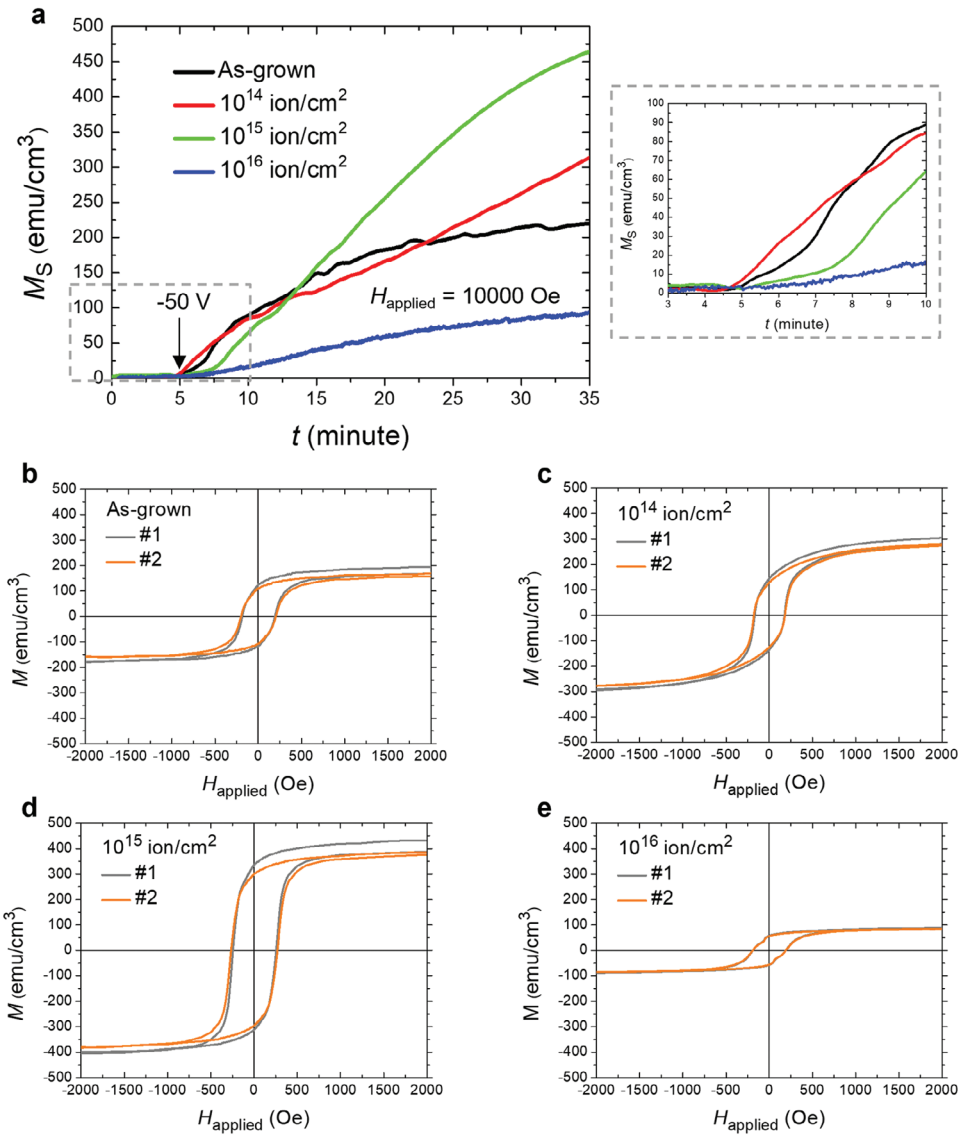

Figure 6. Magneto-ionic behavior by room temperature vibrating sample magnetometry under voltage actuation: a) Time t evolution of saturation magnetization M_S under an external magnetic field of 10 000 Oe ($H_{applied}$) along the plane of the films while applying a voltage of −50 V (covering the time range from 5 to 35 min). b),c), d), and e) are the first two consecutive magnetization versus applied magnetic field curves, M ($H_{applied}$), recorded just after stopping electrolyte-gating the as-grown, and implanted films to 10^{14}, 10^{15}, and 10^{16} ion cm^{-2}, respectively.

magnetic field curves, M ($H_{applied}$), taken just after switching off the applied voltage of as-grown, and implanted films to 10^{14}, 10^{15}, and 10^{16} ion cm^{-2}, respectively. All films exhibit a slight depletion of the induced magnetization upon switching off the applied voltage, which tends to stabilize after the second hysteresis loop measurement (thus after 1 h since each loops takes 30 min to be recorded). In agreement with previously reported results, this process of magnetization depletion somewhat scales with the amount of induced magnetization by magneto-ionic means.[28] As seen in Figure S6 (Supporting Information), although the evolution of coercivity (H_C) and squareness (M_R/M_S) with ion fluence exhibits a complex dependence, the film implanted with 10^{15} ion cm^{-2} shows the most square-shaped hysteresis loops, and the second largest coercivity in agreement with the existence of rather uniform ferromagnetic regions immersed in a residual Co_3O_4 matrix.[43,66]

To further shed light on the magneto-ionic behavior, structural, and compositional measurements of the films upon voltage actuation at −50 V for 30 min have been carried out by high-angle annular dark-field scanning transmission electron microscopy (HAADF-STEM), electron energy loss spectroscopy (EELS) and transmission electron microscopy (TEM). As seen in **Figure 7**, upon voltage actuation, in contrast to the as-grown film, the film implanted with 10^{15} ion cm^{-2} clearly exhibits Co-rich areas (compare Figure 7b with Figure 7f). Moreover, the FFT of the region marked with an orange square corresponding to the high-resolution TEM image of the film implanted with 10^{15} ion cm^{-2} exhibits an additional spot (number 5) corresponding to metallic

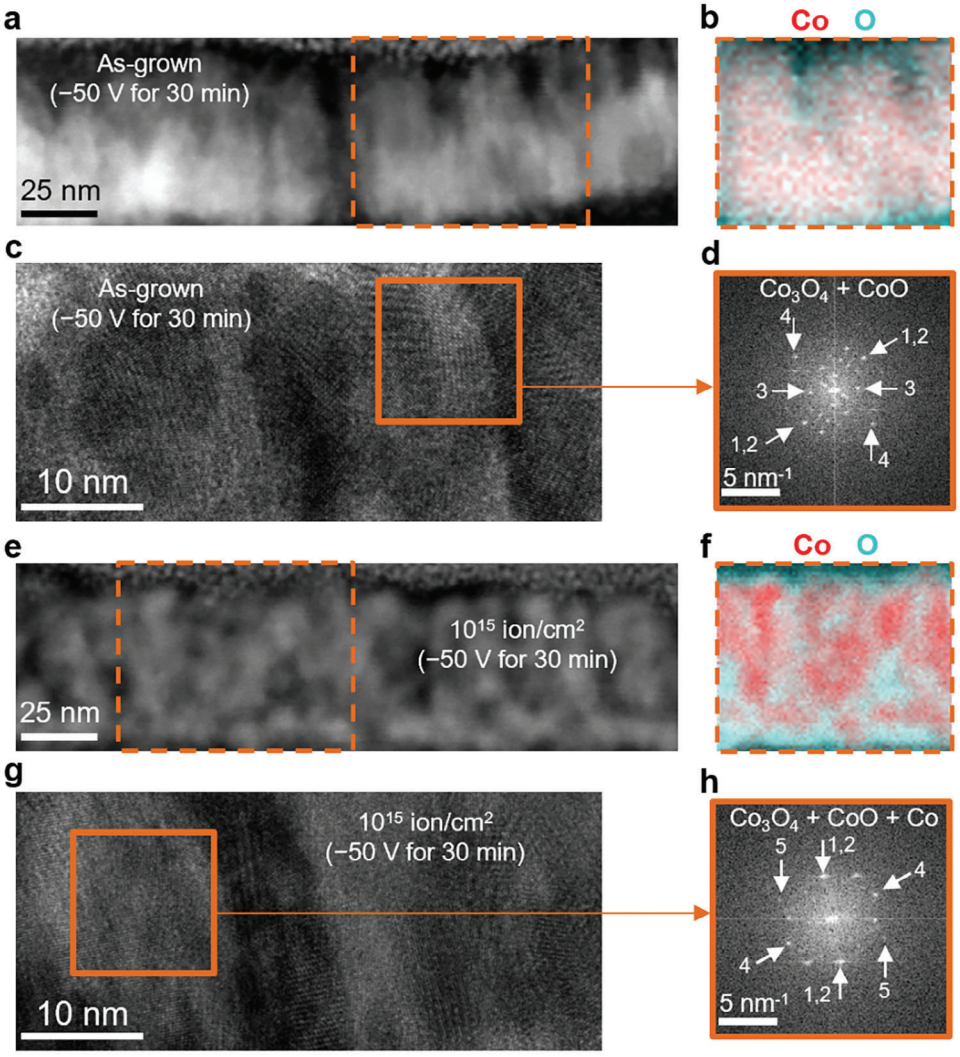

Figure 7. Structural characterization after voltage actuation (−50 V for 30 min) of an as-grown Co_3O_4 film and a film implanted with 5 keV He ions to a fluence of 10^{15} ion cm^{-2} by high-angle annular dark-field scanning transmission electron microscopy (HAADF-STEM), electron energy loss spectroscopy (EELS) and transmission electron microscopy (TEM): a) HAADF-STEM image of the cross-section of an as-grown Co_3O_4 film upon voltage actuation. b) Co and O elemental EELS mappings of the region marked with an orange dashed rectangle in a). c) High-resolution TEM image of a top region of the cross-section of the Co_3O_4 layer. d) Fast Fourier transform of the region marked with an orange square in (c). e) HAADF-STEM image of the cross-section of a Co_3O_4 film implanted to 10^{15} ion cm^{-2} upon voltage actuation. f) Co and O elemental EELS mappings of the region marked with an orange dashed rectangle in (e). g) High-resolution TEM image of a top region of the cross-section of a Co_3O_4 film implanted to 10^{15} ion cm^{-2} upon voltage actuation. h) Fast Fourier transform of the region marked with an orange square in (g). For panels (d) and (h), "1" and "2" spots are in good agreement with (311) Co_3O_4 (PDF 00-009-0418) and (111) CoO (PDF 00-001-1227) interplanar distances (0.244 and 0.245 nm, respectively), while spots "3", "4", and "5" are unambiguously ascribed to (111) Co_3O_4 (PDF 00-009-0418), (200) CoO (PDF 00-001-1227) and (101) hexagonal close packed Co (PDF 00-005-0727) interplanar distances (0.467, 0.212, and 0.191 nm, respectively).

Co, while no traces of it are present in the as-grown film (compare Figure 7d,h). This is consistent with the magnetoelectric measurements, which indicate that, by magneto-ionic means, the film implanted with 10^{15} ion cm^{-2} generates a significantly larger magnetization than the as-grown film (465 vs 220 emu cm^{-3}). The distribution of Co-rich regions embedded in a Co oxide matrix (Figure 7e,f) confirms that, in addition of having O ion migration toward the liquid electrolyte, O ion redistribution inside the film also takes place upon electrolyte gating.

Furthermore, DBVEPAS and VEPALS measurements were carried out upon voltage actuation (**Figure 8**). As seen in Figure 8a, for all films, the S parameter becomes significantly enlarged upon voltage actuation across the whole depth of the films, indicating that voltage-driven ion motion leads to a different structural scenario from a defect viewpoint. The largest increase of defect density after implantation is found for the 10^{15} ion cm^{-2} fluence (the largest absolute increase of *S*). As seen in Figure 8b, defect size becomes slightly increased for the as-grown and the film implanted to the maximum fluence (10^{16} ion cm^{-2}), whereas the films implanted to 10^{14} and 10^{15} ion cm^{-2} exhibit much larger defect sizes upon voltage actuation. This suggests an enhanced magneto-ionic motion in these films, in

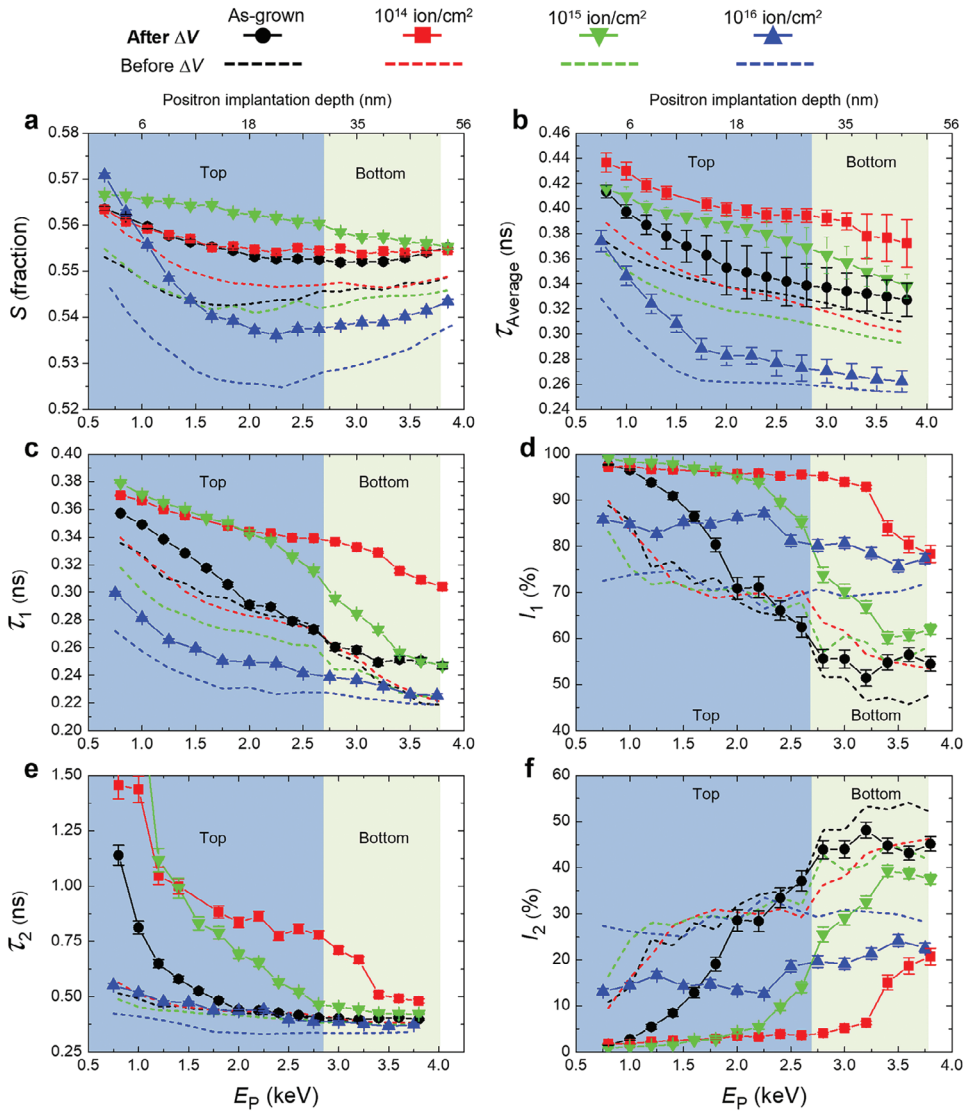

Figure 8. Depth-resolved defect characterization of as-grown and implanted Co_3O_4 films upon voltage actuation (−50 V for 30 min) by Doppler broadening variable energy positron annihilation spectroscopy (DBVEPAS) and variable energy positron annihilation lifetime spectroscopy (VEPALS): a) *S* parameter obtained by DBVEPAS characterization as a function of positron implantation depth which can be also given in positron implantation energy (E_P). See the Experimental Section for further details. b) Average lifetimes obtained by VEPALS as a function of depth. c) and d) are the positron lifetime components 1 (τ_1) and the corresponding relative intensities (I_1), respectively, as a function of positron implantation depth. e) and f) are the positron lifetime components 2 (τ_2) and the corresponding relative intensities (I_2), respectively, as a function of positron implantation depth. To serve as a reference, DBVEPAS and VEPALS characterization of the as-grown and as-implanted films without being subjected to voltage actuation have been also included in the panel in dashed lines. The lines connecting data points are guides to the eye. The blue and green shadings in each panel represent the top and bottom "sublayers" of the 50 nm thick Co_3O_4 film, respectively.

concordance with magnetoelectric measurements, which reveal that these films yield the maximum values of induced magnetization (Figure 6a). Upon looking at the evolution of τ_1 and the corresponding intensity I_1 along depth and comparing the curves with those of the films not subjected to voltage (Figure 8c,d), besides showing in general larger values of defect size (particularly, for the films implanted to 10^{14} and 10^{15} ion cm^{-2}), the I_1 values of these films become above 95% across the top 21 nm (2.2 keV). At further depths, I_1 values start to decrease for the film implanted with 10^{15} ion cm^{-2}, whereas this decrease starts at a depth of ≈39 nm (3.2 keV) for the film implanted with 10^{14} ion cm^{-2}. As seen in Figure 8e,f, the increase in I_1 takes place at the expense of I_2, which becomes significant just at the bottom of the films. Anyhow, small mixed vacancy clusters become the majority defect type upon voltage actuation, suggesting that initial grain boundaries are seeds to initiate diffusion, rapidly transforming into smaller defects with diffusion. The film implanted with 10^{16} ion cm^{-2} shows no significant changes in defect structure after voltage actuation, in agreement with the weak magneto-ionic effect observed in the magnetoelectric measurements. This could be linked to the small size of defects which hamper diffusion but, additionally, to the ion intermixing at the Co_3O_4/Cu

interface, yielding the formation of Cu oxide, eventually degrading the quality of the working electrode, which is known to be crucial to determine the strength of the magneto-ionic effect.

3. Conclusion

Magneto-ionic 50 nm thick Co_3O_4 films with a nanostructured and defective preexisting microstructure were prepared by reactive sputtering. The chosen thickness is the result of the trade-off among various competing effects: the strength of magneto-ionic behavior related to thickness (the thinner the film, the more enhanced magneto-ionic response),[23,30] collisional damage volume (with the aim to controllably modify as much volume of the film as possible) and minimization of atomic intermixing at the film/Cu interface to avoid the degradation of the bottom electrode.[29] Variable energy positron annihilation lifetime spectroscopy experiments revealed that mixed vacancy clusters <10 vacancies are the majority defect type in the as-grown films, and their size decreases with increasing depth from clusters of 10 down to 4 vacancies approximately. To precisely tune the magneto-ionic performance, the as-grown films were then implanted with 5 keV He ions. Due to the stochastic nature of ion implantation,[38] the implantation results in a Gaussian-like depth profile with the maximum collisional damage located at a depth of ≈18 nm, reaching half of this value at a depth of roughly 35 nm, thus leaving the bottom 15 nm of the Co_3O_4 film much less affected than the top counterpart. Thanks to the synergetic effects arising from a nanostructured preexisting microstructure in the as-grown initial films and the subsequent defect engineering achieved through a single implantation process, the magneto-ionic response, in terms of rate and amount of induced magnetization, of the target films at short-, mid-, and long-term voltage actuation is controlled by varying the collisional damage along depth through ion fluence. The defect depth distribution is shown to be crucial to determine the time evolution of the magneto-ionic response since the oxygen ions of the magneto-ionic target become gradually available for diffusion with increasing depth. In general, magneto-ionic effects start from the top surface of the film and, with time, gradually extend toward the inner parts of it. Therefore, the microstructure of the top part of the film rules the magneto-ionic response at the initial stages of voltage actuation, while the bottom region governs the magneto-ionic response at long-term voltage actuation. Considering the as-grown film as a reference, mild collisional damage, characterized by a maximum displacement per atom (dpa) of around 0.01 (achieved upon implanting with 10^{14} ion cm^{-2}), tends to result in slightly larger vacancy clusters along the top 35 nm, thus promoting ion motion at an early stage of voltage actuation. Conversely, intermediate collisional damage with a maximum dpa of roughly 0.1 (achieved upon implanting with 10^{15} ion cm^{-2}) leads to smaller vacancy clusters, thus hindering ion motion at an early stage of voltage actuation. In turn, the density of mixed vacancy clusters increases upon implantation across the bottom 15 nm, leading to a larger number of sites prone to diffuse, which become enabled at long-term voltage actuation. This results in an enhanced induced magnetization. Upon further collisional damage (i.e., implanting to 10^{16} ion cm^{-2}, which yields a maximum dpa of 1), a pronounced defect size reduction occurs. Both effects tend to depress magneto-ionics. The former hinders ion motion to the pronounced decrease in defect size, while the latter promotes ion intermixing with the Cu buffer layer, thus hampering its role as working electrode. This work demonstrates the potential of ion irradiation as a powerful defect-engineering technique that leads to enhanced magneto-ionic effects, with the potential to be used to optimize performance in other iontronic materials. Future works could combine other ion species, energy, fluence, target temperature, and multiple ion implantations to further boost magneto-ionics.

4. Experimental Section

Sample Preparation: Growth of the Magneto-Ionic Targets & Ion Implantation: Fifty nanometers thick Co_3O_4 films were grown by reactive magnetron sputtering on highly conducting B-doped (100)-oriented Si wafers (0.5 mm thick), previously coated with 20 nm of Ti and 60 nm of Cu. Depositions were carried out while partly masking the beneath Cu layer to serve afterward as working electrode. The Co_3O_4 films were grown at room temperature in an AJA International ATC 2400 sputtering system with a base pressure of ≈5×10^{-8} Torr. High-purity O_2 and Ar gases were used. The target-to-substrate distance was ≈11 cm and the deposition rate of about 3 Å s^{-1}. Co_3O_4 was grown using O_2 and Ar flows of 1.7 and 17 sccm, respectively, at a total pressure of 3×10^{-3} Torr, resulting in an O/Ar flow ratio of 9.1%/90.9%.

Then, the as-grown films were uniformly implanted at room temperature with 5 keV He ions at different fluences using a Helium-S system from Spin-Ion Technologies. The implantations were performed with an ion incidence angle of seven with respect to the direction perpendicular to the sample surface to avoid ion channeling. The ion energy of 5 keV was adjusted to have the maximum collisional damage located at a depth ≈18 nm (i.e., within the top "sublayer") to avoid a pronounced atomic intermixing at the Cu interface which could be detrimental to the conductivity of the Cu bottom electrode. This would negatively affect the magneto-ionic performance of the implanted film. Fluences of 10^{14}, 10^{15}, and 10^{16} ion cm^{-2} were used to achieve dissimilar degrees of collisional damage, which expressed as displacement per atom (dpa) was 10^{-2}, 10^{-1}, and 1, respectively. Collisional damage profiles were simulated using the TRIM (TRansport of Ions in Matter) program, which is part of the SRIM (Stopping Range of Ions in Matter) package.[62]

Magnetoelectric Characterization: Magnetoelectric measurements were carried out by performing vibrating sample magnetometry while gating the films at room temperature using a homemade electrolytic cell filled with anhydrous propylene carbonate with solvated Na^+ (in a concentration range of 5–25 ppm) and OH^- ions as liquid electrolyte.[19,28,65] These ionic species originated from treating the propylene carbonate with metallic Na to remove any traces of water. A vibrating sample magnetometer from Micro Sense (LOT-Quantum Design) was used. Measurements of magnetic moment versus time under an external magnetic field of 1 T applied along the film plane (high enough to ensure that the generated ferromagnetic counterpart becomes saturated) were carried out while applying −50 V between the Cu buffer layer, acting as working electrode, and a Pt wire, which acts as counter electrode, using an external Agilent B2902A power supply.[19,28,65] The sign of voltage was such that positive charges accumulated at the counter electrode when a negative voltage is applied. After 30 min, the voltage was switched off and two consecutive hysteresis loops (i.e., magnetization M vs applied magnetic field $H_{applied}$) were measured using a maximum applied magnetic field of 2 T. Taking into account that Co oxides are not ferromagnetic, and the oxygen ion migration does not occur uniformly[28,29] in the systems (see Figure 7e,f), the calculation of the magneto-ionically induced ferromagnetic volume becomes virtually unattainable. Therefore, the induced magnetic moment (arising from the whole investigated sample due to the integral character of vibrating sample magnetometry) is always normalized to the initial volume of the investigated film that is in contact with the liquid electrolyte and, thus, is susceptible to transform to metallic Co. Specifically, the

area of the film in direct contact with the liquid electrolyte is multiplied by the film thickness (i.e., 50 nm). Since the signal arising from the non-ferromagnetic phases (Co oxides, Ti, Cu, and Si) contribute linearly to the induced magnetic moment, the slope of the magnetic moment at applied magnetic fields far above the saturation fields of the induced ferromagnetic phases is subtracted to remove these linear contributions.

Structural and Compositional Measurements: High-resolution transmission electron microscopy (HRTEM), high-angle annular dark-field scanning transmission electron microscopy (HAADF-STEM) and electron energy loss spectroscopy (EELS) were performed on a TECNAI F20 HRTEM /STEM microscope operated at 200 kV. Cross-sectional lamellae were prepared by focused ion beam. The roughness of the surface of the samples have been determined by assessing areas of 250 µm × 190 µm using optical interferometry with a Leica DCM 3D system. While the root mean square (rms) roughness values of the as-grown and all as-implanted films range between 1.8 and 2.1 nm, the rms roughness values of the films treated with −50 V for 30 min fall between 4.1 and 5.1 nm.

Defect Characterization by Doppler Broadening Variable Energy Positron Annihilation Spectroscopy (DBVEPAS) & Variable Energy Positron Annihilation Lifetime Spectroscopy (VEPALS): *DBVEPAS* measurements were conducted at the apparatus for in situ defect analysis AIDA[67] of the slow positron beamline SPONSOR.[68] Positrons are accelerated and monoenergetically implanted into samples in the range between $E_P = 0.05-35$ keV, allowing for depth profiling. A mean positron implantation depth $\langle z \rangle$ (given in nm) can be approximated using a simple material density ρ dependent formula as $\langle z \rangle\ (\text{nm}) = \frac{36}{\rho(\frac{\text{g}}{\text{cm}^3})} E_P(\text{keV})^{1,62}$.[67] This approximation does not account for positron diffusion and gives the best estimation for materials with large defect concentration (short positron diffusion lengths). When implanted into a solid, positrons lose their kinetic energy due to thermalization and, after short diffusion, annihilate in delocalized lattice sites or localize in vacancy-like defects and interfaces emitting usually two anti-collinear 511 keV gamma photons upon meeting electrons. Since, at the annihilation site, thermalized positrons have very small momentum compared to electrons, a broadening of the 511 keV line is observed mostly due to the momentum of electrons, which is measured with high-purity Ge detectors (with an energy resolution of 1.09 keV ± 0.01 keV at 511 keV). This broadening can be defined as a fraction that embraces the middle part of the annihilation line (510.07–511.93 keV) compared to the total spectrum area, which accounts for the so-called *S* parameter. The *S* parameter is the fraction of positrons annihilating with low momentum valence electrons and represents vacancy-type defects and their concentration.

VEPALS measurements were conducted at the Mono-energetic Positron Source (MePS) beamline at Helmholtz-Zentrum Dresden – Rossendorf (Germany)[49] using a digital lifetime $CrBr_3$ scintillator detector, coupled to a Hamamatsu R13089-100 photomultiplier and employing a ADQ14DC-2X digitizer from SPDevices with a 14-bit vertical resolution and a 2GS/s (gigasamples per second) horizontal resolution[50] (total time resolution function down to about 0.24 ns). The resolution function required for spectrum analysis uses two Gaussian functions with different intensities depending on the positron implantation energy, E_P, and appropriate relative shifts. All spectra contained at least 1×10^7 counts. A typical lifetime spectrum $N(t)$ is described by $N(t) = \Sigma(1/\tau_i)I_i \exp(-t/\tau_i)$, where τ_i and I_i are the positron lifetime and intensity of the i-th component, respectively ($\Sigma I_i = 1$). All the spectra were deconvoluted using a non-linear least-squares fitting method employed within the fitting software package PALSfit[51] into three discrete lifetime components, which directly evidence localized annihilation at three different defect types (or sizes: τ_1, τ_2, and τ_3). The corresponding relative intensities reflect to a large extent the concentration of each defect type (size) as long as the size of compared defects is in the similar range. In general, positron lifetime is directly proportional to defects size, that is, the larger the open volume is, the lower probability there is for positrons to be annihilated with electrons, and thereby the longer positron lifetime.[47,48] The positron lifetime and its intensity have been probed as a function of positron implantation energy E_P or, in other words, implantation depth (thickness). The average positron lifetime τ_{Average} is defined as $\tau_{\text{Average}} = \Sigma\tau_i I_i$ and it has a high sensitivity to the defect size (type).

Ab Initio Calculations of Positron Lifetimes: Ab initio calculations of positron lifetimes for different possible defect configurations were performed employing the so-called atomic superposition technique ATSUP.[55] The electron-positron correlations were treated according to Boroński–Nieminen.[56]

Supporting Information

Supporting Information is available from the Wiley Online Library or from the author.

Acknowledgements

Financial support by the European Union's Horizon 2020 Research and Innovation Programme (BeMAGIC European Training Network, ETN/ITN Marie Skłodowska–Curie grant N° 861145), the European Research Council (2021-ERC-Advanced REMINDS Grant N° 101054687), the Spanish Government (PID2020-116844RB-C21 and PDC2021-121276-C31), the Generalitat de Catalunya (2021-SGR-00651) and MCIN/AEI/10.13039/501100011033 & "European Union NextGenerationEU/PRTR" (grant CNS2022-135230) is acknowledged. DBVEPALS and VEPALS were carried out at ELBE from the Helmholtz-Zentrum Dresden – Rossendorf e. V., a member of the Helmholtz Association. The authors would like to thank the facility staff for assistance. This work was partially supported by the Impulse-und Net-working fund of the Helmholtz Association (FKZ VH-VI-442 Memriox), and the Helmholtz Energy Materials Characterization Platform (03ET7015). E. M. is a Serra Húnter Fellow.

Conflict of Interest

The authors declare no conflict of interest.

Data Availability Statement

The data that support the findings of this study are available from the corresponding author upon reasonable request.

Keywords

ion implantation, magneto-ionics, voltage control of magnetism

Received: October 17, 2023
Revised: May 16, 2024
Published online:

[1] R. Ramesh, S. Manipatruni, *Proc. R. Soc. A* **2021**, *477*, 20200942.
[2] *Nat. Electron.* **2018**, *1*, 205.
[3] *Nature* **2018**, *554*, 145.
[4] C. Song, B. Cui, F. Li, X. Zhou, F. Pan, *Prog. Mater. Sci.* **2017**, *87*, 33.
[5] J.-M. Hu, C.-W. Nan, *APL Mater.* **2019**, *7*, 080905.
[6] A. Molinari, H. Hahn, R. Kruk, *Adv. Mater.* **2019**, *31*, 1806662.
[7] M. Nichterwitz, S. Honnali, M. Kutuzau, S. Guo, J. Zehner, K. Nielsch, K. Leistner, *APL Mater.* **2021**, *9*, 030903.
[8] J. de Rojas, A. Quintana, G. Rius, C. Stefani, N. Domingo, J. L. Costa-Krämer, E. Menéndez, J. Sort, *Appl. Phys. Lett.* **2022**, *120*, 070501.

[9] A. J. Tan, M. Huang, C. O. Avci, F. Büttner, M. Mann, W. Hu, C. Mazzoli, S. Wilkins, H. L. Tuller, G. S. D. Beach, *Nat. Mater.* **2019**, *18*, 35.
[10] M. Gößler, M. Albu, G. Klinser, E.-M. Steyskal, H. Krenn, R. Würschum, *Small* **2019**, *15*, 1904523.
[11] G. Chen, C. Ophus, A. Quintana, H. Kwon, C. Won, H. Ding, Y. Wu, A. K. Schmid, K. Liu, *Nat. Commun.* **2022**, *13*, 1350.
[12] N. Lu, Z. Zhang, Y. Wang, H.-B. Li, S. Qiao, B. Zhao, Q. He, S. Lu, C. Li, Y. Wu, M. Zhu, X. Lyu, X. Chen, Z. Li, M. Wang, J. Zhang, S. C. Tsang, J. Guo, S. Yang, J. Zhang, K. Deng, D. Zhang, J. Ma, J. Ren, Y. Wu, J. Zhu, S. Zhou, Y. Tokura, C.-W. Nan, J. Wu, et al., *Nat. Energy* **2022**, *7*, 1208.
[13] G. Chen, M. Robertson, M. Hoffmann, C. Ophus, A. L. Fernandes Cauduro, R. Lo Conte, H. Ding, R. Wiesendanger, S. Blügel, A. K. Schmid, K. Liu, *Phys. Rev. X* **2021**, *11*, 021015.
[14] M. Huang, M. U. Hasan, K. Klyukin, D. Zhang, D. Lyu, P. Gargiani, M. Valvidares, S. Sheffels, A. Churikova, F. Büttner, J. Zehner, L. Caretta, K.-Y. Lee, J. Chang, J.-P. Wang, K. Leistner, B. Yildiz, G. S. D. Beach, *Nat. Nanotechnol.* **2021**, *16*, 981.
[15] S. Dasgupta, B. Das, M. Knapp, R. A. Brand, H. Ehrenberg, R. Kruk, H. Hahn, *Adv. Mater.* **2014**, *26*, 4639.
[16] S. Dasgupta, B. Das, Q. Li, D. Wang, T. T. Baby, S. Indris, M. Knapp, H. Ehrenberg, K. Fink, R. Kruk, H. Hahn, *Adv. Funct. Mater.* **2016**, *26*, 7507.
[17] X. Zhu, J. Zhou, L. Chen, S. Guo, G. Liu, R.-W. Li, W. D. Lu, *Adv. Mater.* **2016**, *28*, 7658.
[18] M. Ameziane, J. Huhtasalo, L. Flajšman, R. Mansell, S. van Dijken, *Nano Lett.* **2023**, *23*, 3167.
[19] J. de Rojas, A. Quintana, A. Lopeandía, J. Salguero, B. Muñiz, F. Ibrahim, M. Chshiev, A. Nicolenco, M. O. Liedke, M. Butterling, A. Wagner, V. Sireus, L. Abad, C. J. Jensen, K. Liu, J. Nogués, J. L. Costa-Krämer, E. Menéndez, J. Sort, *Nat. Commun.* **2020**, *11*, 5871.
[20] J. de Rojas, J. Salguero, F. Ibrahim, M. Chshiev, A. Quintana, A. Lopeandia, M. O. Liedke, M. Butterling, E. Hirschmann, A. Wagner, L. Abad, J. L. Costa-Krämer, E. Menéndez, J. Sort, *ACS Appl. Mater. Interfaces* **2021**, *13*, 30826.
[21] J. De Rojas, J. Salguero, A. Quintana, A. Lopeandia, M. O. Liedke, M. Butterling, A. G. Attallah, E. Hirschman, A. Wagner, L. Abad, J. L. Costa-Krämer, J. Sort, E. Menéndez, *Phys. Rev. Appl.* **2021**, *16*, 034042.
[22] Z. Tan, S. Martins, M. Escobar, J. de Rojas, F. Ibrahim, M. Chshiev, A. Quintana, A. Lopeandia, J. L. Costa-Krämer, E. Menéndez, J. Sort, *ACS Appl. Mater. Interfaces* **2022**, *14*, 44581.
[23] Z. Tan, J. de Rojas, S. Martins, A. Lopeandia, A. Quintana, M. Cialone, J. Herrero-Martín, J. Meersschaut, A. Vantomme, J. L. Costa-Krämer, J. Sort, E. Menéndez, *Mater. Horiz.* **2023**, *10*, 88.
[24] C. J. Jensen, A. Quintana, P. Quarterman, A. J. Grutter, P. P. Balakrishnan, H. Zhang, A. V. Davydov, X. Zhang, K. Liu, *ACS Nano* **2023**, *17*, 6745.
[25] U. Bauer, L. Yao, A. J. Tan, P. Agrawal, S. Emori, H. L. Tuller, S. van Dijken, G. S. D. Beach, *Nat. Mater.* **2015**, *14*, 174.
[26] D. A. Gilbert, A. J. Grutter, E. Arenholz, K. Liu, B. J. Kirby, J. A. Borchers, B. B. Maranville, *Nat. Commun.* **2016**, *7*, 12264.
[27] F. Ibrahim, A. Hallal, B. Dieny, M. Chshiev, *Phys. Rev. B* **2018**, *98*, 214441.
[28] A. Quintana, E. Menéndez, M. O. Liedke, M. Butterling, A. Wagner, V. Sireus, P. Torruella, S. Estradé, F. Peiró, J. Dendooven, C. Detavernier, P. D. Murray, D. A. Gilbert, K. Liu, E. Pellicer, J. Nogues, J. Sort, *ACS Nano* **2018**, *12*, 10291.
[29] J. de Rojas, A. Quintana, A. Lopeandía, J. Salguero, J. L. Costa-Krämer, L. Abad, M. O. Liedke, M. Butterling, A. Wagner, L. Henderick, J. Dendooven, C. Detavernier, J. Sort, E. Menéndez, *Adv. Funct. Mater.* **2020**, *30*, 2003704.
[30] S. Martins, J. de Rojas, Z. Tan, M. Cialone, A. Lopeandia, J. Herrero-Martín, J. L. Costa-Krämer, E. Menéndez, J. Sort, *Nanoscale* **2022**, *14*, 842.
[31] Z. Tan, Z. Ma, L. Fuentes, M. Oskar Liedke, M. Butterling, A. G. Attallah, E. Hirschmann, A. Wagner, L. Abad, N. Casañ-Pastor, A. F. Lopeandia, E. Menéndez, J. Sort, *ACS Nano* **2023**, *17*, 6973.
[32] D. A. Gilbert, J. Olamit, R. K. Dumas, B. J. Kirby, A. J. Grutter, B. B. Maranville, E. Arenholz, J. A. Borchers, K. Liu, *Nat. Commun.* **2016**, *7*, 11050.
[33] S. Vasala, A. Jakob, K. Wissel, A. I. Waidha, L. Alff, O. Clemens, *Adv. Electron. Mater.* **2020**, *6*, 1900974.
[34] J. Dabrowski, *Solid State Phenom.* **2000**, *71*, 23.
[35] A. Atkinson, C. Monty, in *Surfaces and Interfaces of Ceramic Materials*, Vol. *173* (Eds: L.-C. Dufour, C. Monty, G. Petot-Ervas), NATO ASI Series, Springer, Berlin New York **1989**.
[36] R. Wang, X. Chen, Z. Huang, J. Yang, F. Liu, M. Chu, T. Liu, C. Wang, W. Zhu, S. Li, S. Li, J. Zheng, J. Chen, L. He, L. Jin, F. Pan, Y. Xiao, *Nat. Commun.* **2021**, *12*, 3085.
[37] A. Baktash, B. Demir, Q. Yuan, D. J. Searles, *Energy Storage Mater.* **2021**, *41*, 614.
[38] M. Nastasi, J. W. Mayer, *Ion Implantation and Synthesis of Materials*, Springer, Berlin, New York **2006**.
[39] J. Fassbender, D. Ravelosona, Y. Samson, *J. Phys. D: Appl. Phys.* **2004**, *37*, R179.
[40] C. Chappert, H. Bernas, J. Ferré, V. Kottler, J.-P. Jamet, Y. Chen, E. Cambril, T. Devolder, F. Rousseaux, V. Mathet, H. Launois, *Science* **1998**, *280*, 1919.
[41] J. Fassbender, M. O. Liedke, T. Strache, W. Möller, E. Menéndez, J. Sort, K. V. Rao, S. C. Deevi, J. Nogués, *Phys. Rev. B* **2008**, *77*, 174430.
[42] E. Menéndez, J.-C. Stinville, C. Tromas, C. Templier, P. Villechaise, J.-P. Rivière, M. Drouet, A. Martinavičius, G. Abrasonis, J. Fassbender, M. D. Baró, J. Sort, J. Nogués, *Appl. Phys. Lett.* **2010**, *96*, 242509.
[43] E. Menéndez, J. Demeter, J. Van Eyken, P. Nawrocki, E. Jedryka, M. Wójcik, J. F. Lopez-Barbera, J. Nogués, A. Vantomme, K. Temst, *ACS Appl. Mater. Interfaces* **2013**, *5*, 4320.
[44] H. Modarresi, V. Lazenka, E. Menéndez, M. Lorenz, M. Bisht, A. Volodin, C. Van Haesendonck, M. Grundmann, M. J. Van Bael, K. Temst, A. Vantomme, *J. Phys. D: Appl. Phys.* **2016**, *49*, 325302.
[45] R. Juge, K. Bairagi, K. G. Rana, J. Vogel, M. Sall, D. Mailly, V. T. Pham, Q. Zhang, N. Sisodia, M. Foerster, L. Aballe, M. Belmeguenai, Y. Roussigné, S. Auffret, L. D. Buda-Prejbeanu, G. Gaudin, D. Ravelosona, O. Boulle, *Nano Lett.* **2021**, *21*, 2989.
[46] C. J. Jensen, A. Quintana, M. Sall, L. Herrera Diez, J. Zhang, X. Zhang, D. Ravelosona, K. Liu, *J. Magn. Magn. Mater.* **2021**, *540*, 168479.
[47] R. Krause-Rehberg, H. Leipner, *Positron Annihilation in Semiconductors: Defect Studies*, Springer, Berlin, New York **1999**.
[48] F. Tuomisto, I. Makkonen, *Rev. Mod. Phys.* **2013**, *85*, 1583.
[49] A. Wagner, M. Butterling, M. O. Liedke, K. Potzger, R. Krause-Rehberg, *AIP Conf. Proc.* **2018**, *1970*, 040003.
[50] E. Hirschmann, M. Butterling, U. Hernandez Acosta, M. O. Liedke, A. G. Attallah, P. Petring, M. Görler, R. Krause-Rehberg, A. Wagner, *J. Instrum.* **2021**, *16*, P08001.
[51] J. V. Olsen, P. Kirkegaard, N. J. Pedersen, M. Eldrup, *Phys. Status Solidi C* **2007**, *4*, 4004.
[52] P. J. Schultz, K. G. Lynn, *Rev. Mod. Phys.* **1988**, *60*, 701.
[53] C. H. Hodges, M. J. Stott, *Solid State Commun.* **1973**, *12*, 1153.
[54] C. Hugenschmidt, *Surf. Sci. Rep.* **2016**, *71*, 547.
[55] M. J. Puska, R. M. Nieminen, *J. Phys. F: Met. Phys.* **1983**, *13*, 333.
[56] E. Boroński, R. M. Nieminen, *Phys Rev B* **1986**, *34*, 3820.
[57] B. Barbiellini, M. J. Puska, T. Torsti, R. M. Nieminen, *Phys Rev B* **1995**, *51*, 7341.
[58] S. Prucnal, R. Gago, D. G. Calatayud, L. Rebohle, M. O. Liedke, M. Butterling, A. Wagner, M. Helm, S. Zhou, *J. Phys. Chem. C* **2023**, *127*, 12686.

[59] H. Bola George, D. P. Hoogerheide, C. S. Madi, D. C. Bell, J. A. Golovchenko, M. J. Aziz, *Appl. Phys. Lett.* **2010**, *96*, 263111.
[60] A. Fellman, A. E. Sand, J. Byggmästar, K. Nordlund, *J. Phys.: Condens. Matter* **2019**, *31*, 405402.
[61] S. Agarwal, M. O. Liedke, A. C. L. Jones, E. Reed, A. A. Kohnert, B. P. Uberuaga, Y. Q. Wang, J. Cooper, D. Kaoumi, N. Li, R. Auguste, P. Hoseman, L. Capolungo, D. J. Edwards, M. Butterling, E. Hirschmann, A. Wagner, F. A. Selim, *Sci. Adv.* **2020**, *6*, eaba8437.
[62] The TRIM (Transport of Ions in Matter) program is included in the SRIM (Stopping Range of Ions in Matter) package (SRIM-2016), http://srim.org/ (accessed: January 2023).
[63] R. Krause-Rehberg, V. Bondarenko, E. Thiele, R. Klemm, N. Schell, *Nucl. Instrum. Meth. B* **2005**, *240*, 719.
[64] C. Leighton, *Nat. Mater.* **2019**, *18*, 13.
[65] C. Navarro-Senent, A. Quintana, E. Menéndez, E. Pellicer, J. Sort, *APL Mater.* **2019**, *7*, 030701.
[66] D. L. Leslie-Pelecky, R. D. Rieke, *Chem. Mater.* **1996**, *8*, 1770.
[67] M. O. Liedke, W. Anwand, R. Bali, S. Cornelius, M. Butterling, T. T. Trinh, A. Wagner, S. Salamon, D. Walecki, A. Smekhova, H. Wende, K. Potzger, *J. Appl. Phys.* **2015**, *117*, 163908.
[68] W. Anwand, G. Brauer, M. Butterling, H. R. Kissener, A. Wagner, *Defect Diffus. Forum* **2012**, *331*, 25.